ARCHIVES OF MECHANICS
Arch. Mech. **71** (4–5), 507–526, 2019, DOI: 10.24423/aom.3162

Experimental determination and numerical simulation of material and damage behaviour of 3D printed polyamide 12 under quasi-static loading

D. SCHOB[1)], R. ROSZAK[1,3)], I. SAGRADOV[1)], H. SPARR[1)], M. ZIEGENHORN[1)], A. KUPSCH[2)], F. LÉONARD[2)], B.R. MÜLLER[2)], G. BRUNO[2)]

[1)] *Brandenburg University of Technology Cottbus-Senftenberg, 01968 Senftenberg, Germany*

[2)] *BAM, Bundesanstalt für Materialforschung und -prüfung, 12200 Berlin, Germany*

[3)] *Poznan University of Technology, 60-965 Poznan, Poland, e-mail: Robert.Roszak@b-tu.de*

In order to characterise the material and damage behaviour of additively manufactured polyamide 12 (PA12) under quasi-static load and to implement it in a numerical model, experiments under quasi-static load as well as microstructural investigations were carried out. Selective laser sintering (SLS) was used as the manufacturing process. For the classification of the material behaviour, quasi-static cyclic tests with holding times as well as tensile tests were performed. X-ray refraction and computed tomography (CT) were used to investigate the damage behaviour. The Chaboche model, which has already been applied for metallic materials under thermomechanical loading, served as the basis for the selection of the numerical material model. The same procedure was used for the selection of the damage model, where the Gurson–Tvergaard–Needleman (GTN) model was chosen, which was already used for porous metallic materials. The Chaboche model shows very good agreement with experimental results. Furthermore, the coupling with the GTN model allows a very good modelling of the damage behaviour. Finally, it could be shown that the selected models are suitable to simulate the material and damage behaviour of 3D printed PA12.

Key words: polyamide 12, 3D printing, viscoplastic, Chaboche model, damage, GTN model, X-ray refraction, computed tomography.

1. Introduction

Technological progress requires the development of new materials. The development also involves the evaluation of their performance. More and more often design materials, plastics and metals are made with AM (additive manufacturing) technology. For practical applications, the 3D printed parts should withstand various amounts of mechanical and environmental stresses during their service life. It is important to know the required strengths for each application

under various loading conditions, and at the very least, the physical properties of 3D-printed parts should be similar to those manufactured by conventional methods, such as injection moulding. While AM provides the opportunity to quickly step forward from design to product especially for parts that are difficult or impossible to machine, challenges remain for predicting the mechanical performance [1]. The AM process of depositing layers of polymeric material results in structural components with anisotropic properties and residual stress, which is a major challenge. Researchers and Original Equipment Manufacturers (OEMs) must establish standardised methods of determining material properties from AM processing rather than the mechanical properties of a particular design. Very few papers highlight the complexity in related material properties, AM mesostructure, and part design for standardised testing. Despite the importance of this problem for the success of AM, the literature available in this field is sparse [2]. AM is the most appropriate technique for fast creating structural components and enables building complex parts, which could not be created with traditional technologies, like injection moulding process.

Investigations already carried out on metallic materials produced conventionally and additively have shown that it is possible, on the one hand, to develop material models for quasi-static loading and, on the other hand, to convert information on the inhomogeneous material structures obtained from X-ray refraction and CT analysis into a numerical model, [3, 4, 5]. Therefore, the approach of this paper is to investigate existing material and damage models of metals and transfer them to additively manufactured PA12.

For the description of the material behaviour, a quasi-static cyclic test with implemented holding times as well as tensile tests were tested. For the description of the damage behaviour, X-ray refraction and computed tomography were carried out. With the results from the experimental part, the material and damage parameters of the selected numerical models could be determined and verified. For the numerical description of the material behaviour, the Chaboche model was applied, which was already used for metallic materials under thermomechanical loading. The Gurson–Tvergaard–Needleman model, which was used for porous metallic materials, served as the basis for the choice of the damage model. By coupling the Chaboche and GTN model it is possible to cover the material behaviour of the 3D printed PA12 and the damage behaviour considering the microstructure.

2. Experimental part

2.1. Sample preparation according to standards

The selective laser sintering (SLS) method was used to create specimens for the experiments. A sPro 230 printer from 3D Systems was used. It was run with

a laser power of 70 W, a scanning speed of 10 m/s for the filling and 5 m/s for the contour, and a layer thickness of 0.08–0.15 mm. The temperature of the printing chamber and the process was 170°C and 200°C, respectively. In this work, 3D printed specimens of PA12 were investigated. PA12 is a semi-crystalline thermoplastic material and commonly used for SLS printing.

Currently, 47 standards exist for polymers, but only 20 of them can be used with restrictions and the others are not usable [2]. Therefore, the geometry of the specimens was chosen according to DIN EN ISO 527-2 [6], Fig. 1a. All samples were printed as shown in Fig. 1b. With the manufactured samples, quasi-static cyclic tests (Sec. 2.2) and tensile tests (Sec. 2.3) were carried out.

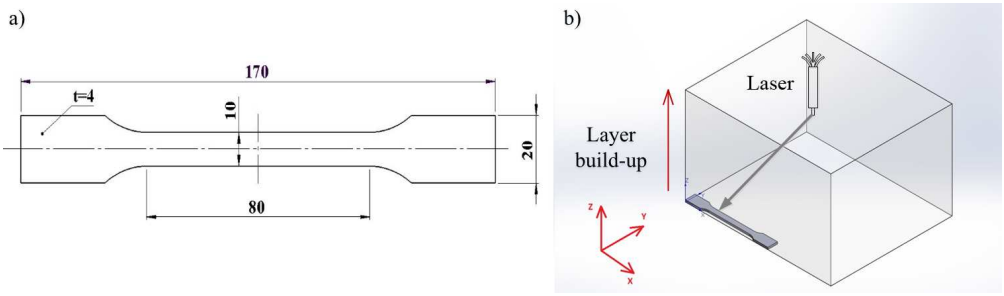

FIG. 1. Specimen: a) dimension of specimen, b) single printing layers are in the xy-plane, the build-up direction of the layers is the z-direction.

2.2. Quasi-static load

The characterisation of the material started with a quasi-static cyclic test, which included holding times at different displacement levels. This procedure was proposed by HAUPT [7]. The holding times is chosen to 1000 s followed by change of displacement with a speed of 5 mm/min to the next level and the procedure is repeated, Fig. 2.

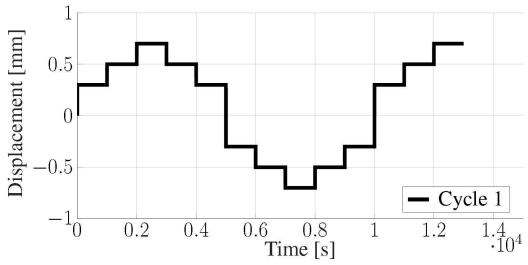

FIG. 2. Conditions for the quasi-static cyclic test with holding times at different displacement levels.

This type of test enables classifying the materials with respect to their rate-dependent and rate-independent behaviour. The rate-dependent material behaviour distinguishes two classes: viscoelastic and viscoplastic materials. Experimentally, viscoplasticity is characterized by an equilibrium hysteresis, obtained from connecting the stress-strain pairs, measured at the endpoints of holding times. In case of viscoelasticity, this procedure gives an equilibrium line.

2.3. Tensile test

After the investigation of the material classification, tensile tests were performed with new specimens. Seven tensile tests at a displacement rate of 5 mm/min were done with a testing machine of Hegewald & Peschke - Inspekt-Table 10 kN at 23°C, according to DIN EN ISO 527-2 [6]. The deformation of the specimens has been traced by a 3D Digital Image Correlation (DIC) technique.

2.4. Digital image correlation

For the Digital Image Correlation (DIC), an ARAMIS 3D Camera measuring system was used for full area and point based measurements. DIC is a non-contact optical full-field measurement of deformations. A reference image serves as the basis for the measurement of deformations. For this reason, a unique black and white pattern is sprayed onto the virgin specimen. The stochastic patterns are used to identify discrete image areas, that are determined by analysing image information with the subpixel accuracy. With this method, point and area measurement results are generated and used in materials research and component testing to determine the static behaviour of samples.

The basic correlation function is described by:

$$C(x,y,u,v) = \sum_{i,j=-N/2}^{N/2} (I(x+i,y+j) - I^*(x+u+i,y+v+j))^2, \tag{2.1}$$

where C is a function of x and y, which are the coordinates of the reference image. The displacement and disparity are defined as u and v, respectively. I is the image before deformation and is a function of the pixel values $x+i$ and $y+j$. I^* is the image according to the correlation and is a function of the pixel values with the applied displacements. The whole function C is actually the sum of the squared differences between the reference image and the deformed image, whereby the function is summed over the subset size N. By loading the geometry data into the program, it is possible to analyse the normal stress in the tensile direction (x-direction in Fig. 1b) using the measured deformations.

2.5. Scanning electron microscopy

The scanning electron microscope (SEM) utilizes a focused beam of high-energy electrons to generate surface images of solid samples. Signals resulting from the interactions between electrons and samples provide information about the sample, to include external morphology, chemical composition, and crystalline structure and orientation of the material. Conventional SEM techniques provide fields of view ranging from 1cm to 5 μm, corresponding to magnifications of 20× to 30.000×. Here, magnifications of 40× for the whole fracture surface and 150× for an analyse of an edge area were used.

In order to specify the pore size and the location more precisely, X-ray refraction and computed tomography (CT) were performed with a virgin (V) specimen and a sample of the tensile test (T).

2.6. X-Ray refraction

X-ray refraction [8] is employed as a scanning technique to extract the spatially resolved internal relative specific surface [9]. It has been successfully applied to characterize pore size distributions, interface orientations, e.g. of ceramics [10, 11, 12]. It is based on the deflection of X-rays at inner surfaces in complete analogy to the refraction of visible light at interfaces of media having different refraction indices, numerically expressed by Snell's law. As a major difference, the X-ray refraction index $n = 1 - \delta$ (δ being the refraction decrement in the order of 10^{-7} to 10^{-6}) is slightly smaller than unity. This implies on the one hand, the inversion of focusing properties [13] and very small scattering angles (some seconds to minutes of arc) with the critical angle Θ_{crit} of total reflection as the upper limit ($\Theta_{crit} = \sqrt{2\delta}$). In the case of the investigated polyamide, using Mo-Kα radiation (17.4 keV), δ is $7.72 \cdot 10^{-7}$, resulting in $\Theta_{crit} = 4.5$ arcmin. Although the spatial resolution of the scanning measurement is limited by the incident beam cross section (500 × 40 μm^2), the technique is sensitive to any surface of pores, cracks or material interfaces down to the nanometer size region. Rather than imaging individuals the result of the measurement is the specific surface, i.e., the density of (oriented) surfaces integrated over the gauge volume (500 μm × 40 μm × thickness of the specimen).

For the X-ray refraction measurements, an approximately 25 mm long piece was cut from the measuring length of a tensile and virgin specimen and examined with the following experimental set-up. The experimental equipment consists of a standard fine structure X-ray generator (operated at $U = 40$ kV, $I = 0.8$ mA) providing nearly monochromatic radiation (Mo-Kα). The refraction effect was measured using a modified small-angle scattering X-ray camera of the Kratky type collimation in combination with two scintillation detectors. This allows for

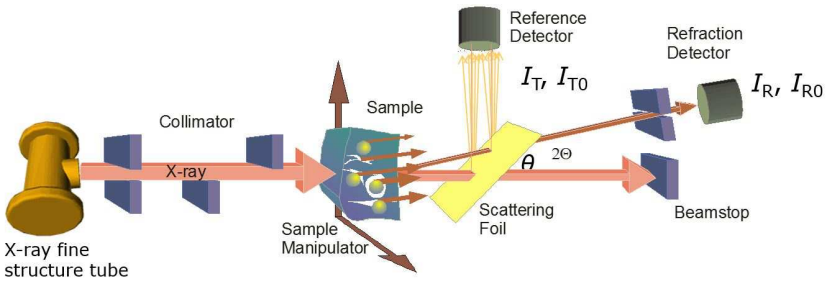

Fig. 3. Laboratory set-up of the scanning X-ray refraction technique [12].

the simultaneous detection of the X-ray refraction intensity I_R and the transmitted intensity I_T behind the sample, Fig. 3.

By measuring the two intensities with and without (index 0) a specimen in the beam, one obtains the so-called refraction value $C_m \cdot D$:

$$C_m \cdot D = \frac{I_R/I_{R0}}{I_T/I_{T0}} - 1, \tag{2.2}$$

where D is the sample thickness. For the derivation of Eq. (2.2), the reader is referred to [14]. Usually, I_T and I_{T0} are used to calculate the absorption property $\mu \cdot D = -\ln(I_T/I_{T0})$, μ being the linear attenuation coefficient. With priorly known μ_0 (tabulated or reference data) and macroscopic thickness D (measured), the porosity p is estimated as:

$$p = 1 + \ln\left(\frac{I_T}{I_{T0}}\right)/(\mu_0 \cdot D). \tag{2.3}$$

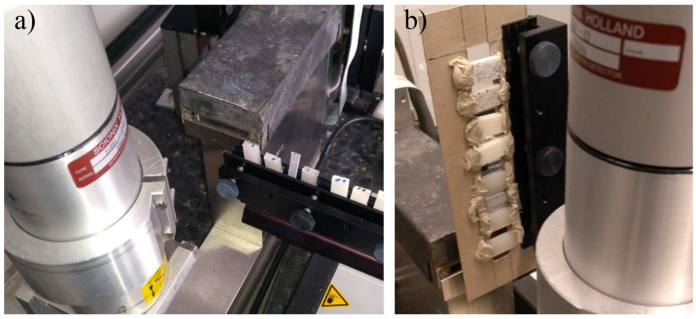

Fig. 4. Detail of the experimental set-up with samples mounted a) horizontally ($Q \| Td$, sensitive for transverse surfaces) and b) vertically ($Q \perp Td$, sensitive for axial surfaces), Q pointing upwards in both measurements.

Since the X-ray refraction strongly depends on the orientation of the surfaces, the measurements were performed with the tensile direction Td of the samples (x in Fig. 1b) parallel and perpendicular to the scattering vector Q of the camera system. A detail of the experimental setup with the two types of mounting is shown in Fig. 4: in a) horizontal mounting: $Q \uparrow$ and $Td \uparrow$ (giving $C_m \cdot D_{par}$) and in b) vertical sample mounting: $Q \uparrow$ and $Td \rightarrow$ (giving $C_m \cdot D_{perp}$).

2.7. Computed tomography

In order to be able to describe the sizes of the pores as well as the pore distribution also qualitatively, computed tomography analyses (CT) were carried out. For this purpose, pieces of about $5 \times 5 \times 5$ mm^3 in size were taken from the border within the measuring length of a tensile and virgin specimen. The specimens were scanned on a GE v|tome|x L 180/300 equipped with a 180 kV transmission target (tungsten thin film onto diamond window). The X-ray tube was operated under 50 kV and 150 µA. The two specimens were stacked on top of each other and 3 scans were acquired over the full height of the stack. The voxel size was 8 µm, the integration time was 2000 ms per projection, with 3142 projections for each 360° rotations, Fig. 5.

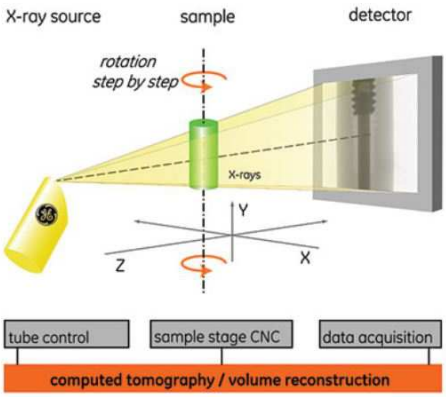

FIG. 5. Schematic diagram of an X-ray computed tomography system [15].

The raw CT data was reconstructed using GE proprietary reconstruction software. Then the CT data was processed, analysed, and visualised with Thermo Fischer Scientific Avizo software (version 9.4) [16]. The pores were separated from the polymer matrix based on their greyscale value in the reconstructed CT volume. This operation is called segmentation and a threshold value was selected according to Otsu's method, [17]. The assessment of the porosity content value as a function of the selected threshold value was estimated by measuring the

evolution of the porosity content by varying the threshold. A variation of ±500 greyscale values (CT data were 16 bit data, ranging from 0 to 65535) resulted in a porosity content variation of ±0.2%.

3. Results

3.1. Material behaviour

3.1.1. Quasi-static test. For the classification of the material, the results of quasi-static cyclic tests with holding times were used. Figure 6 illustrates results of the cyclic test and an equilibrium hysteresis (dotted line). This is the first evidence of viscoplastic material behaviour.

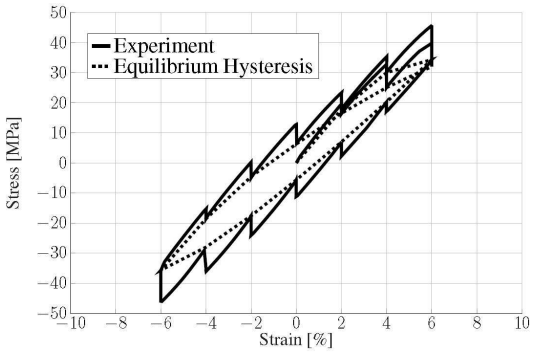

Fig. 6. Results of cyclic tests with holding times. Solid line: experimental technical stress-strain data, dotted line: connecting the end points of the holding times results in an equilibrium hysteresis.

3.1.2. Tensile test. Tensile tests were carried out to investigate the mechanical properties. Three of seven specimens failed and broke outside of the measuring length. The results of the four valid tests are shown in the technical stress-strain diagram, Fig. 7. The mean values of the material properties and their standard deviation obtained from the tensile tests are listed in Table 1.

Table 1. Mean values and standard deviation.

	Mean value	Standard deviation
Young's Modulus [MPa]	1604.25	29.72
Elongation at break [%]	7.42	0.25
Ultimate tensile strength [MPa]	40.62	1.39

The quasi-static cyclic tests with holding times clearly showed viscoplastic material behaviour of additively manufactured PA12. The same behaviour could already be observed for aluminium and cast iron in previous studies [18, 19].

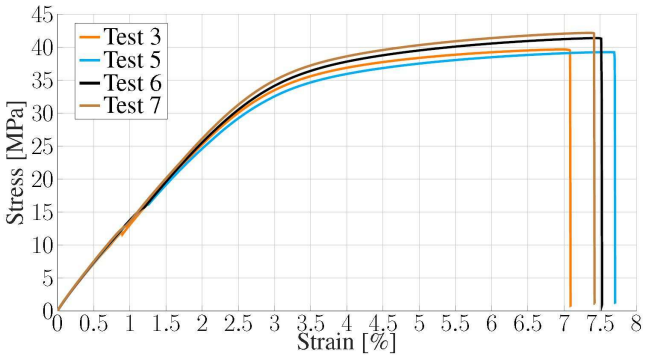

FIG. 7. Results of tensile test PA12, $v = 5$ mm/min, at 23°C.

Furthermore, the characteristic material properties could be determined by the tensile tests, as well as brittle material behaviour without a pronounced yield strength. These results are the basis for the selection of the material model, which is described in detail in Section 4.1.

3.2. Damage behaviour

3.2.1. Scanning electron microscopy. To describe the damage behaviour, the microstructure of fracture surfaces of the specimens were examined by means of a scanning electron microscope (SEM) after the tensile tests, Fig. 8. The specimens do not have a homogeneous material structure and contain pores. In the fringe area, it was found that the printing process does not produce a smooth surface and that small notches are formed on the surface.

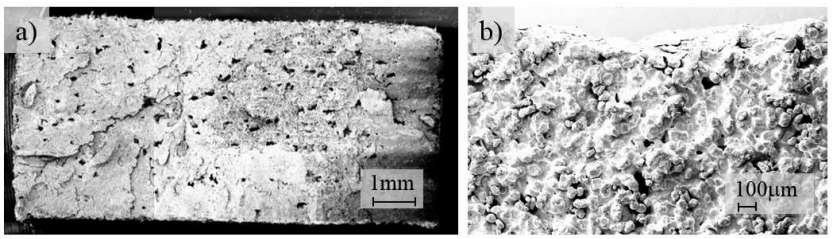

FIG. 8. Scanning electron micrographs, [20] a) fracture surface 40× magnification, b) Section of the upper edge area, 150× magnification.

3.2.2. X-Ray refraction. Figures 9 and 10 show the results of the refraction measurement. Figure 9 depicts the topographs of $C_m \cdot D_{par}$ (left) and $C_m \cdot D_{perp}$ (right, rotated 90° with respect to the measurement). The transmission measurements in horizontal orientations of the samples are shown in Figs. 11 and 12.

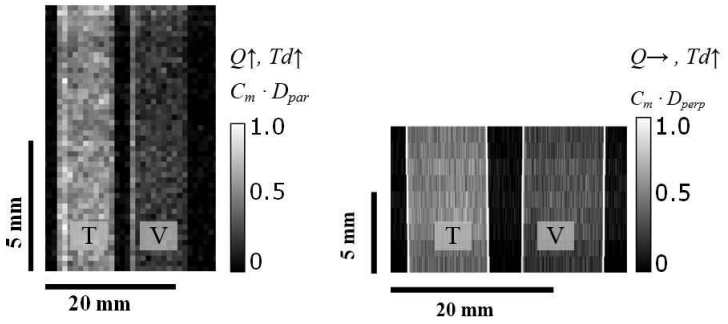

Fig. 9. $C_m \cdot D$ topographs obtained from horizontally (left) and vertically (right) mounted samples: V: virgin, T: tensile loaded. The different pixel size (scan increments) is due to the beam cross section (see above). The directions of scattering (Q) and tensile (Td) are indicated.

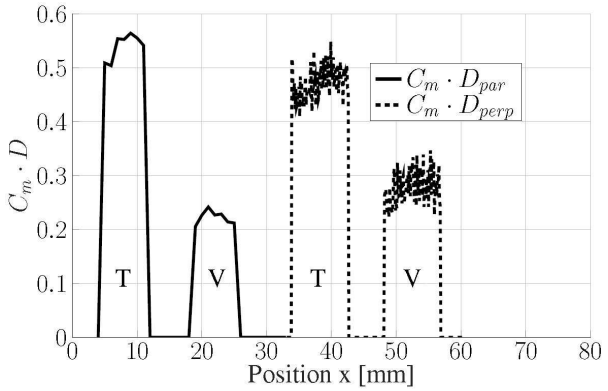

Fig. 10. Cumulative $C_m \cdot D$ profiles of samples T and V in both orientations, revealing the significantly higher specific surface in T.

The samples show distinct refraction signals. In the virgin state, the refraction values $C_m \cdot D_{par} = 0.23$ and $C_m \cdot D_{perp} = 0.27$ indicate internal surfaces, which are attributed to pores. They show a small anisotropy (elongation in the tensile direction). The tensile loaded specimen exhibits refraction values 0.54 and 0.47, respectively, almost twice as large as the virgin sample. Since porosity does not change, the additional internal surface is supposed to be due to cracks. $C_m \cdot D_{par} > C_m \cdot D_{perp}$ indicates that they are preferentially oriented perpendicularly to the tensile direction (i.e. oriented along the transverse direction, y in Fig. 1b).

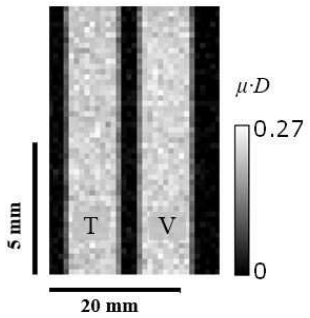

FIG. 11. $\mu \cdot D$ topographs of samples T and V (obtained from horizontal mounting).

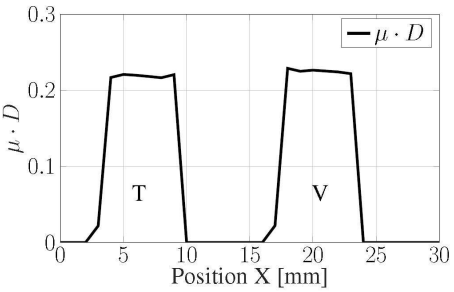

FIG. 12. Cumulative $\mu \cdot D$ profiles of samples T and V.

3.2.3. X-Ray computed tomography. Figure 13 shows the generated CT images of the virgin and tensile specimen. A porosity of 3.7% of the virgin and 3.6% of the tensile samples was measured. The distribution of the cavities over the specimen is very uniform, so that no stronger melting of the surfaces and edges can be expected due to the printing process.

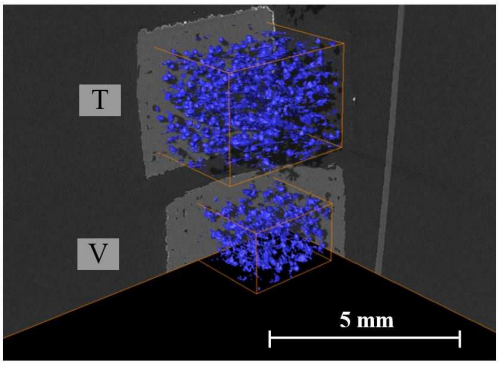

FIG. 13. 3D CT rendering of porosity (blue) for virgin (V, bottom) and tensile (T, top) specimens, with 2D orthoslices in the background (grey).

Within the investigated components, pores of different shapes occurred. These were classified according to their sphericity. Pores with a more spherical shape have a small shape factor and pores with a large aspect ratio or small roundness have large shape factors. Figure 14 shows a selection of measured pore shapes. From left to right, the shape factor increases, i.e. the pores' resemblance to spheres decreases.

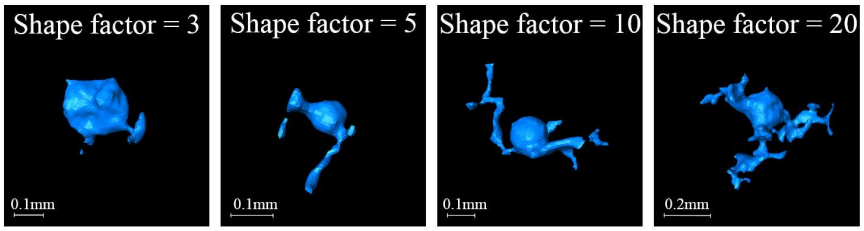

Fig. 14. Selection of pore shapes. From left to right, the shape factor increases, which distinguishes the shape more and more from a sphere.

Furthermore, the CT measurement has shown an increase of spherical shapes from the virgin to the tensile loaded specimen, Fig. 15. In the virgin state (blue dots), more pores of larger shape factor are identified. After tensile loading (red dots), the shape factors of the pores become smaller, indicating that the pores become more spherical. In addition, a bimodal pore size distribution is observed. The analysis exhibits a minimum at 100 µm (equivalent diameter). The tensile specimen contains a larger portion of small pores. This tendency is in accordance with the refraction results. Considering the large pore size fraction, the center of gravity shifts from 191 µm (for V) to 171 µm (for T).

The porosity content values obtained from the CT analysis are smaller than those obtained from X-ray transmission (Table 2). However, the CT results are comparable to the closed porosity values obtained by Dupin *et al.* [21] for laser sintered parts made of Duraform PA 12. While the CT value is limited by the spatial resolution (voxel size 8 µm), X-ray transmission is sensitive to any size of pores. Beyond size, the latter is an average porosity, irrespective of closed or open pores.

Table 2. Porosity of virgin and tensile specimen calculated from X-ray transmission.

Type of test	$p_{X\text{-}ray}$ (%)	p_{CT} (%)
Virgin	5	3.7
Tensile	4	3.6

Both X-ray refraction and CT analysis have shown that 3D printed materials already exhibit porosity in their virgin state. The pores are distributed homogeneously. For the simulations, spherical cavities were initially assumed

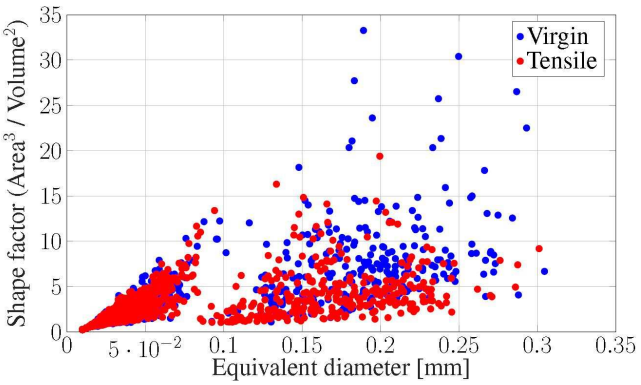

FIG. 15. Scatter plot of the pore shape factor as a function of equivalent diameter of the virgin specimen (blue dots) and after tensile load (red dots). The density of scatter points indicates the bimodal size distribution, the decrease of the shape factor after tensile load and that the average pore diameter in a range of 0.1 to 0.3 mm becomes smaller.

as damage. The selected damage model, which is described in more detail in Section 4.2, is also based on this assumption.

3.2.4. Digital image correlation For the DIC evaluation, the normal stress in the tensile direction was selected. In Fig. 16a, the analysed area is indicated in the virgin state. At about 3.7% strain, first indications of shear bands are observed (Fig. 16b). During further tensile load, at about 7.4% strain (immediate before the fracture), the shear bands are clearly marked (Fig. 16c).

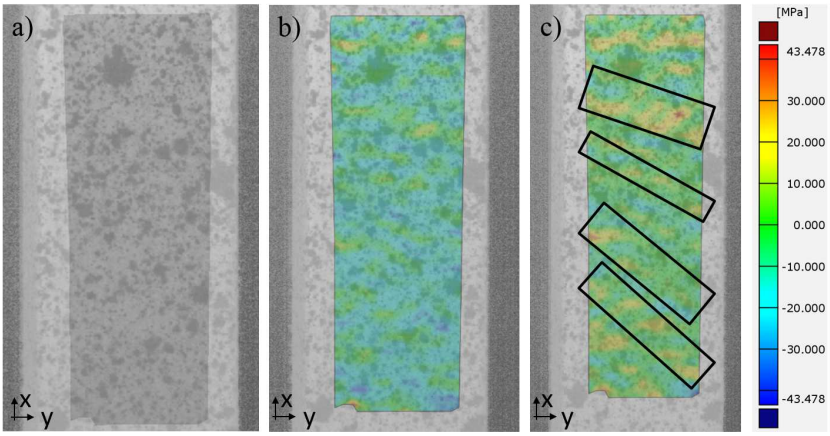

FIG. 16. Results of digital image correlation – normal stress in x-direction, a) virgin state, dark grey marked area is the selected investigation area, b) at 3.7% elongation, c) at 7.4% of elongation.

This shear band formation is typical for semi-crystalline polymers [22]. They usually occur at an angle of 30–45°. Shear flow for semi-crystalline plastics is achieved by sliding, twin formation and martensite-like transformations. Such phenomena can also be observed in other crystalline solids.

4. Numerical simulation

4.1. Material model by Chaboche

Based on the experimental results (sec. 3.1), a material model was selected and the simulation was performed. The numerical analysis allows calculations for complex geometries using data from experimental studies to describe the material. The purpose of numerical analysis is to establish the correlation of the results obtained from the experiment with the numerical simulation. Reaching convergent results allows to adapt complex material models to the behaviour of the material. This enables analysis of more sophisticated geometric models in a complex load scenario in the future. A variety of existing material models were examined and discussed with respect to their applicability to additively manufactured plastics. As described in Section 3.1, additively manufactured PA12 exhibits viscoplastic behaviour. For metals behaving like viscoplastics, the Chaboche model was used in the past, e.g. [18]. Applying the material model in presence of a thermomechanical influence, e.g. cast iron (GJS, GJV, GJL [23]) or cast aluminium alloys [19] is one of many examples, for which this model can be used. Therefore, this work deals with the development of material specific fitting of the material model by Chaboche – and a limitation on purely isothermal experiments at 23°C. The Chaboche model is composed of a differential equation system. The origin of this model is the subdivision of the total strain rate $\dot{\boldsymbol{\varepsilon}}^{tot}$ into an elastic $\dot{\boldsymbol{\varepsilon}}^{el}$ and a viscoplastic $\dot{\boldsymbol{\varepsilon}}^{vp}$ part. Here, the definition of the viscoplastic strain rate is decisive. This consists of the viscoplastic multiplicator $\dot{\lambda}$ and the direction $\boldsymbol{n}$. The flow function φ is the closure of the elastic domain. The flow function depends on the one hand, on the yield stress σ_y, the deviatoric stress s and on the other hand, on the kinematic hardening. The kinematic hardening is taken into account by the back stresses $\dot{\alpha}_i$. This is described by the accumulated plastic strain $\dot{p}$ and the hardening parameters C and γ.

$$\dot{\boldsymbol{\varepsilon}}^{tot} = \dot{\boldsymbol{\varepsilon}}^{el} + \dot{\boldsymbol{\varepsilon}}^{vp}, \tag{4.1}$$

$$\dot{\boldsymbol{\sigma}} = E(\dot{\boldsymbol{\varepsilon}}^{el}) = E(\dot{\boldsymbol{\varepsilon}}^{tot} - \dot{\boldsymbol{\varepsilon}}^{vp}), \tag{4.2}$$

$$\dot{\boldsymbol{\varepsilon}}^{vp} = \dot{\lambda} \cdot \boldsymbol{n} = \dot{\lambda} \left\{ \frac{\partial \varphi}{\partial \sigma} \right\} = \sqrt{\frac{2}{3} \boldsymbol{\varepsilon}^{vp} : \boldsymbol{\varepsilon}^{vp}} \frac{3}{2} \frac{\boldsymbol{s} - \sum_{i=1}^{n} \boldsymbol{\alpha_i}}{\sigma_y}, \tag{4.3}$$

$$\dot{\boldsymbol{\alpha}}_i = \frac{2}{3} C_i \dot{\boldsymbol{\varepsilon}}^{vp} - \gamma_i \alpha_i \dot{p}. \tag{4.4}$$

The Chaboche model described here contains three parameters in its original form, which are determined experimentally. These are the Young's modulus E and the two hardening parameters γ_i and C_i. Depending on how many back stresses are used, the number of parameters changes. Best results could be achieved with two back stresses and thus a total of five parameters. The parameters were adjusted by a fitting tool [24]. Afterwards, the parameters were implemented in Ansys and the numerical simulation was carried out.

4.2. Damage model by Gurson–Tvergaard–Needleman

Since the CT results (Sec. 3.2.3.) suggest to assume spherical pores, the damage model of Gurson–Tvergaard–Needleman [25] was applied. TVERGAARD and NEEDLEMAN [25] extended the model of GURSON [26] in 1984. The extended model considers growth, nucleation and coalescence. Based on the experimental results and microstructural analysis, coalescence was not considered in this paper. Thus, the GTN model used, is composed of the following Eqs. (4.6) to (4.10) for strain controlled nucleation.

$$\varphi = \frac{\sigma_{eq}^2}{\sigma_y^2} + 2q_1 f \cosh\left(\frac{3q_2}{2}\frac{\sigma_{kk}}{\sigma_y}\right) - 1 - q_1^2 (f)^2, \tag{4.5}$$

$$\dot{f} = \dot{f}_{growth} + \dot{f}_{nucleation}, \tag{4.6}$$

$$\dot{f}_{growth} = (1-f)\dot{\varepsilon}^{pl} : I, \tag{4.7}$$

$$\dot{f}_{nucleation} = \frac{f_N \dot{\bar{\varepsilon}}^{pl}}{S_N\sqrt{2\pi}}\, e^{-\frac{1}{2}\left(\frac{\bar{\varepsilon}^{pl}-\varepsilon_N}{S_N}\right)^2}, \tag{4.8}$$

$$\dot{f}_0 = \dot{f}(t=0). \tag{4.9}$$

The flow function φ is defined by von Mises equivalent stress σ_{eq}, two Tvergaard–Needleman parameters q_1 and q_2, effective hydrostatic stress σ_{kk} and the void volume fraction f. The void volume fraction is the summation of growth and nucleation. Nucleation is regulated by the maximum void fraction for nucleated voids f_N, effective plastic strain $\bar{\varepsilon}^{pl}$, rate of the effective plastic strain $\dot{\bar{\varepsilon}}^{pl}$, mean strain ε_N and the deviation S_N.

For the numerical simulation, the porosity of the virgin sample is needed. This was measured in an initial porosity f_0 at time $t = 0$. Due to the different values for the initial porosity of the X-ray refraction and CT analysis, the average of both analyses was taken for the initial porosity and amounts to 4.7%. In addition to the initial porosity, q_1, q_2, f_N, ε and S_N have been determined as damage parameters with an own fitting tool. The optimized parameters were also implemented in Ansys 17.2. The adapted material and damage parameters are shown in Table 3.

Table 3. Adapted material and damage parameters.

		Unit	Chaboche	Chaboche+GTN
Young's Modulus	E	[MPa]	1450	1450
Poisson ratio	μ		0.4	0.4
Yield Stress	σ_F	[MPa]	17.50	17.50
Hardening parameter	C_1	[MPa]	7920.469	7920.5
Hardening parameter	γ_1		387.81	387.81
Hardening parameter	C_2	[MPa]	600.026	600.026
Hardening parameter	γ_2		63.986	63.986
1. Tvergaard–Needleman constant	q_1		–	1.2
2. Tvergaard–Needleman constant	q_2		–	1.1
Initial porosity	f_0		–	0.047
Nucleation porosity	f_N		–	0.12
Mean strain	ε_n		–	0.15
Strain standard deviation	S_N		–	0.06

4.3. Validation of models

Based on the experimental results, the Chaboche material model as well as the damage model were adapted. Tensile test 6 (see Fig. 7) was selected as a basis for the fitting procedure. Figure 17 shows the result of test 6 (black solid line) compared to the adapted Chaboche model (blue dotted line).

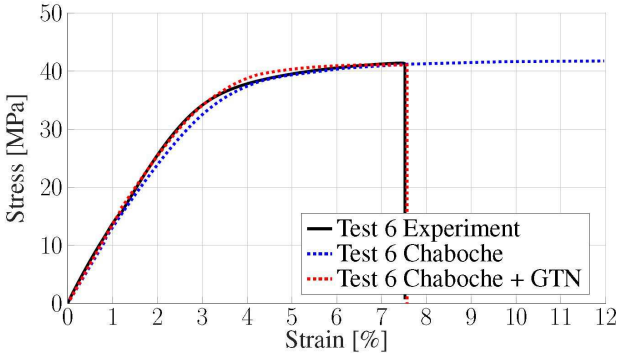

Fig. 17. Results of the numerical simulation compared with experimental technical stress-strain data of the tensile test. The largest deviation between Experiment and numerical simulation is 1.6 MPa for Chaboche model and 1.4 MPa for the coupled Chaboche+GTN model.

Using solely the Chaboche model, the material behaviour is described very well, but it is not possible to simulate the fracture at the measured strain. Therefore, the Chaboche and the GTN model were coupled. The coupled model enabled to find a good agreement for both the material and the damage behaviour, Fig. 17.

Figure 18 shows the results of the normal stress in x-direction. A homogeneous stress field develops when the Chaboche model is used solely (Fig. 18a). When coupling the Chaboche and GTN models, an inhomogeneous stress field with shear bands is observed (Fig. 18b). Similar results were obtained from (experimental) digital image correlation (Fig. 16).

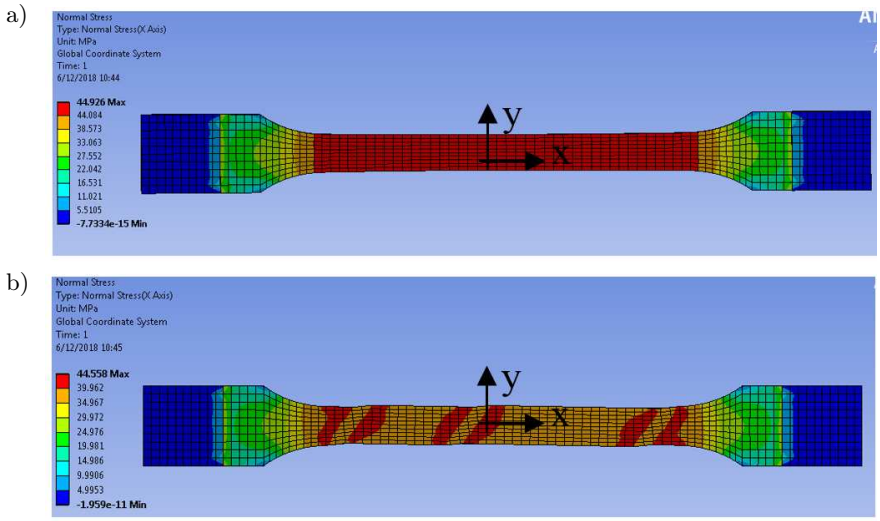

FIG. 18. Using the Chaboche model, a homogeneous stress field is created in the numerical simulation (a), which cannot represent the development of shear bands. By coupling the Chaboche and GTN models (b), it is also possible to image shear bands that became visible in the experiment (see Fig. 16c) and thus take the microstructure into account.

5. Discussion

The purpose of this study was to characterize additively manufactured PA12 under quasi-static loading and to develop a material and damage model based on experimental investigations of the microstructure. The results have shown that the viscoplastic material behaviour can be mapped very well with the selected Chaboche law, which has already been applied to metallic materials. The coupling of the Chaboche approach with the damage model of Gurson–Tvergaard–Needleman also resulted in a very good agreement between experiment and numerics. Furthermore, microstructural investigations have shown that pores and cavities occur inside the material and that the surface has a high roughness due to the manufacturing process.

A crucial point was to decide whether the material behaviour of the 3D printed PA12 can be reproduced with a viscoplastic material model. Through the quasi-static cyclic tests with holding times according to HAUPT [7], on the one hand, viscoplastic material behaviour could be determined and on the

other hand, a very good agreement between experiment and numerics could be achieved by the selection of the Chaboche model. Thus, it can be ascertained that the material model according to Chaboche can be used for simulation of the material behaviour of 3D printed PA12.

A further focus of the investigations was to determine whether the selected damage model of Gurson–Tvergaard–Needleman properly describes the results of the microstructural investigations. The GTN model assumes spherical pores. Indeed, pore shape factors, extracted from CT results, indicate a preferred occurrence of nearly spherical pores. However, in addition to the spherical pores, other possible damage initiators could be involved. On the one hand, X-ray refraction indicated the occurrence of additional surfaces preferentially oriented perpendicular to the tensile direction. Other thermoplastic polymers (such as polyethylene (PE) and polypropylene (PP)) are known to show cavitation under tensile load [27]. Cavitations are small elongated voids formed in the amorphous region between crystals. At small strains, those cavitations are located at polar parts of spherulithes and are oriented perpendicular to the tensile direction. On the other hand, SEM images revealed a considerable surface roughness, which can promote notch effects.

In summary, it can be stated that, although only spherical voids have been assumed as damage initiators, very good results have been achieved between experiment and numerics. At this stage, it cannot be quantified to which extent cavities have an influence on the damage.

The validation of the experimental results and the adaptation of the material and damage model showed that the material and damage behaviour of 3D printed PA12 can be mapped by Chaboche and GTN models under quasi-static loading.

6. Outlook

In future studies, it will be investigated, whether the Chaboche and GTN models can be applied to additively manufactured plastic components under cyclic loading. Alternatively, different models, e.g., the Bodner-Partom model [28] or suited modifications of the current model are evaluated. Furthermore, the temperature as load or as self-heating influence, which plays a crucial role in cyclic tests for polymers, is to be implemented in the numerical model. With a focus on the damage initiators, it should also be determined whether a different damage model, where cavities and notch effects are taken into account, is better suited. In connection with this, various production parameters (such as laser power, laser displacement speed, slip distance and pressure pattern) will be systematically examined with regard to various load scenarios (static, cyclic, relaxation). In addition, the relative alignment of the assembly and load directions will be varied.

References

1. J.R. DIZON, A.H. ESPERA, Q.CHIEN, R.C. ADVINCULA, *Mechanical characterization of 3d-printed polymers*, *Additive Manufacturing*, **20**, 44–67, 2018.
2. A. M. FORSTER, *Materials Testing Standards for Additive Manufacturing of Polymer Materials*, Additive Manufacturing, 2015.
3. C. LANDRON, E. MAIRE, O. BOUAZIZ, J. ADRIEN, L. LECARME, A. BAREGGI, *Validation of void growth models using x-ray microtomography characterization of damage in dual phase steels*, Acta Materialia, **59**, 7564–7573, 2011.
4. CH. ANGERMEIER A.M. HORR, *An innovative use of ct method in light metals development*, ICT Conference Proceedings, Acta Materialia, 149–157, 2014.
5. G. ZIÓŁKOWSKI, E. CHLEBUS, P. SZYMCZYK, J. KURZAC, *Application of x-ray ct method for discontinuity and porosity detection in 316l stainless steel parts produced with slm technology*, Archives of Civil and Mechanical Engineering, **14**, 4, 608–614, 2014.
6. DIN Deutsches Institut für Normung e.V., DIN EN ISO 527-2: Kunststoffe – Bestimmung der Zugeigenschaften, Teil 2: Prüfbedingungen für Form- und Extrusionsmassen, 2012.
7. P. HAUPT, *Continuum Mechanics and Theory of Materials*, Springer, Berlin, Heidelberg, 2002.
8. M.P. HENTSCHEL, R. HOSEMANN, A. LANGE, B. UTHER, R. BRÜCKNER, *Röntgenkleinwinkelbrechung an Metalldrähten, Glasfäden und hartelastischem Polypropylen*, Acta Crystallographica, **A 43**, 506–513, 1987.
9. M.P. HENTSCHEL, K.-W. HARBICH, D. EKENHORST, J. SCHORS, *Röntgentopographie der Faser- und Polymerorientierung*. Materialprüfung, **39**, 121–123, 1997.
10. A. KUPSCH, A. LANGE, M.P. HENTSCHEL, Y. ONEL, T. WOLK, A. STAUDE, K. EHRIG, B.R. MÜLLER, G. BRUNO, *Evaluating porosity in cordierite-based diesel particulate filter materials. Part 1. X-ray refraction*, Journal of Ceramic Science and Technology, **4**, 169–176, 2013.
11. A. KUPSCH, B.R. MÜLLER, A. LANGE, G. BRUNO, *Microstructure characterization of ceramics via 2d and 3d x-ray refraction techniques*, Journal of the European Ceramic Society, **37**, 1879–1889, 2017.
12. B.R. MÜLLER, R.C. COOPER, A. LANGE, A. KUPSCH, M. WHEELER, M.P. HENTSCHEL, A. STAUDE, A. PANDEY, A. SHYAM, G. BRUNO, *Stress-induced microcrack density evolution in β-eucryptite ceramics: experimental observations and possible route to strain hardening*, Acta Materialia, **144**, 627–641, 2018.
13. S. EVSEVLEEV, B.R. MÜLLER, A. LANGE, A. KUPSCH, *Refraction driven x-ray caustics at curved interfaces*, Nuclear Instruments and Methods in Physics Research, **A 916**, 275–282, 2019.
14. F.E. FENSCH-KLEEMANN, K.W. HARBICH, M.P. HENTSCHEL, *Microstructural characterisation of porous ceramics by x-ray refraction topography*, **79**, 11, 35–38, 2002.
15. O. BRUNKE, *Industrial x-ray ct: Quality control from the lab to the production floor*, Quality Magazine, 2015.
16. Thermo Fischer Scientific. *Thermo fischer scientific avizo software* (version 9.4).

17. N. Otsu, *A thresholding selection method from grayscale histogram*, IEEE Transactions on Systems, Man, and Cybernetics, **9**, 1, 62–66, 1979.

18. J.-L. Chaboche, *Constitutive equations for cyclic plasticity and cyclic viscoplasticity*, International Journal of Plasticity, **5**, 3, 247–302, 1989.

19. O. S. Hopperstad, M. Langseth, S. Remseth, *Cyclic stress-strain behaviour fo alloy aa6060, part I: Uniaxial experiments and modelling*, International Journal of Plasticity, **11**, 725–739, 1995.

20. R. Franke, D. Schob, M. Ziegenhorn, *Additive Fertigung von Bauteilen und Strukturen: Prüfverfahren und numerische Simulation von mechanischen Eigenschaften 3D-gedruckter thermoplastischer Kunststoffe*, H.A. Richard, B. Schramm and T. Zipsner (Hrsg): Additive Fertigung von Bauteilen und Strukturen, Springer, Wiesbaden, 137–158, 2017.

21. S. Dupin, O. Lame, C. Barres, J.-Y. Charmeau, *Microstructural origin of physical and mechanical properties of polyamide 12 processed by laser sintering*, European Polymer Journal, **48**, 9, 1611–1621, 2012.

22. W. Grellmann S. Seidler, *Kunststoffprüfung*, Carl Hanser Verlag München, **3**, 146, 2015.

23. M. Metzger, B. Nieweg, C. Schweizer, T. Seifert, *Lifetime prediction of cast iron materials under combined thermomechanical fatigue and high cycle fatigue loading using a mechanism-based model*, International Journal of Fatigue, **53**, 58–66, 2013.

24. University of Technology Brno. *Fitting tool hyperfit.*

25. V. Tvergaard, A. Needleman, *Analysis of the cup cone fracture in a round tensile bar*, Acta Metallurgica, **32**, 1, 1984.

26. A.L. Gurson, *Continuum theory of ductile rupture by void nucleation and growth-i. yield criteria and flow rules for porous ductile media*, Journal of Engineering Materials and Technology, **1982**, 18, 1982.

27. A. Pawlak, A. Gałęski, *Cavitation during tensile drawing of semicristalline polymers*, Polymery, **9**, 627–636, 2011.

28. S.R. Bodner, I. Partom, Y. Partom, *Uniaxial cyclic loading of elastic-viscoplastic materials*, Journal of Applied Mechanics, **46**, 4, 805–810, 1979.

Received December 7, 2018; revised version April 10, 2019.
Published online August 6, 2019.